

HiSST: 4th International Conference on High-Speed Vehicle Science Technology 22 -26 September 2025, Tours, France



Leading-Edge Shape Effects on Hypersonic Crossflow Receptivity to Slow Acoustic Waves in Swept Flat Plates

Lin Han¹, Caihong Su²

Abstract

This study investigates the effects of leading-edge shape on hypersonic crossflow receptivity to slow acoustic waves in a Mach 6 flow over swept flat plates. Three leading-edge geometries are examined: a cylindrical nose (with sharp curvature discontinuity) and two ellipsoidal noses (with smoother curvature transitions), designed to examine how geometric features—bluntness and nose-body junction abruptness—influence the excitation and evolution of crossflow traveling modes. Direct numerical simulations (DNS), combined with linear stability theory (LST) and parabolized stability equations (PSE), are used to resolve the receptivity process and downstream disturbance development for a target traveling mode. The steady base flow analysis shows that increased nose bluntness leads to a larger favorable pressure gradient, which consequently results in greater amplification of the crossflow instability mode as predicted by LST. DNS reveals that the traveling mode is excited primarily within the rapidly varying mean flow region near the leading edge. Importantly, the abrupt curvature discontinuity of the cylindrical nose induces localized scattering effects on disturbances, while ellipsoidal noses mitigate this scattering due to their gradual curvature transitions. Receptivity coefficients indicate that the cylindrical nose exhibits smaller values compared to the ellipsoidal cases. However, this reduced initial amplitude of the traveling mode through receptivity is offset by enhanced downstream instability amplification. Specifically, the stronger pressure gradient associated with the cylindrical nose promotes faster disturbance growth, ultimately leading to larger disturbance amplitudes downstream.

Keywords: Hypersonic, Boundary layer, Receptivity, Crossflow, Traveling mode

Nomenclature

A – Perturbation amplitude

a – Aspect ratio of model

p – Pressure

u – Chordwise velocity

v – Wall normal velocity

w - Spanwise velocity

T – Temperature

 β – Spanwise wavenumber

 ρ – Density

 ω – Angular frequency

Superscripts

′ – Perturbation

Subscripts

1. Introduction

The boundary-layer transition is a critical issue in high-speed aircraft design due to its substantial impact on skin friction and surface heat flux, significantly influencing aerodynamic performance and thermal protection systems [1]. This process begins with low-level background disturbances and evolves through receptivity, exponential growth of linear instability modes, and nonlinear breakdown. Among these, receptivity—where external disturbances excite instability modes—sets the initial conditions for subsequent growth and remains poorly understood despite advances in linear stability theory.

HiSST-2025-XXXX Page | 1 Leading-Edge Shape Effects on Hypersonic Crossflow Receptivity to Slow Acoustic Waves in Swept Flat Plates Copyright © 2025 by author(s)

¹ Tianjin university, 92 Weijin Rd, Nankai district, Tianjin, China, linhan@tju.edu.cn

² Tianjin university, 92 Weijin Rd, Nankai district, Tianjin, China, su_ch@tju.edu.cn

In hypersonic flows, previous receptivity studies have largely focused on two-dimensional or axisymmetric boundary layers (e.g., flat plates, wedges, cones), where the Mack second mode is dominant [2]. However, under swept or inclined flow conditions, crossflow instability often becomes the primary transition mechanism. Typical configurations for crossflow research include yawed cones [3], elliptic cones [4], and swept wings [5]. The crossflow velocity profile is highly unstable and can support both stationary and traveling waves. While stationary waves dominate in low-turbulence environments, traveling modes grow more significant under higher disturbance levels [6], and have been frequently observed in recent hypersonic wind tunnel tests [7] and flight experiments [8]. A key question is how these traveling modes are excited by freestream disturbances—a central focus of this study.

Flight vehicles often incorporate blunt noses to mitigate heat loads, a feature that may be enhanced by ablation. For 2D or axisymmetric boundary layers, small bluntness generally stabilizes the flow and delays transition [9]. In contrast, studies on swept wings show that bluntness promotes crossflow transition at high sweep angles, though it can delay transition where the Mack mode dominates [10]. Recent studies on cones at angle of attack present mixed results: some experiments suggest that larger bluntness delays transition [11], while computational work indicates that increased nose radius suppresses the growth of crossflow instabilities [12].

Most prior numerical studies have emphasized stability effects rather than receptivity. This work aims to address that gap by investigating the receptivity of traveling crossflow modes over swept flat plates with varying nose bluntness—comparing a blunter cylindrical nose with two sharper elliptical shapes. We seek to clarify how nose shape affects receptivity mechanisms and the subsequent development of traveling crossflow waves. The paper is structured as follows: Section 2 outlines the methodology; Section 3 describes the models and computational setup; Section 4 presents base flows and linear stability results; Section 5 discusses receptivity outcomes and the influence of nose bluntness; and Section 6 provides a summary.

2. Computational setup

We consider the excitation of a traveling mode in hypersonic flow over a swept flat plate. Typical wind tunnel flow conditions are considered as provided in Table 1. The Mach number Ma_{∞} is 6, and the swept angle Λ is 45°. The freestream temperature T_{∞} and velocity Q_{∞} are 60.98 K and 939.18 m/s, respectively. The unit Reynolds number Re_{∞} based on freestream quantities is 3×10^7 m⁻¹. The wall is considered to be isothermal with a temperature of 300 K. Under the assumption of the perfect gas, the specific heat ratio and the Prandtl number are taken as $\gamma=1.4$ and $\gamma=0.72$, respectively.

*Ma*_∞ Λ (°) T_{∞} (K) Q_{∞} (m/s) Re_{∞} (m⁻¹) $T_{\rm W}$ (K) 6 45 60.98 939.18 3×10⁷ 300

Table 1. Flow conditions.

The flat plate under investigation consists of a/an cylindrical/elliptical nose and a tangent flat plate, as illustrated in Fig. 1. The nose can be formulated as follows:

$$\frac{(x-a)^2}{a^2} + \frac{y^2}{b^2} = 1$$
 (1)

where a and b represent the horizontal and vertical semi-axes of the ellipse, respectively. Clearly, b equals half the plate thickness of 10 mm, which serves as the length scale for this study. Three different nose geometries are considered, with dimensionless a=1, 3, and 5, respectively. The case with a=1 represents a more blunt cylindrical nose, while a=3 and 5 correspond to two less blunt ellipsoidal noses.

The computational setup is illustrated in Fig. 2, with (x, y, z) and (ξ, η, ζ) denoting the global Cartesian and body-fitted coordinate systems, respectively. Since the flat plate considered has an infinite span, the base flow variables are independent of the coordinate z. Therefore, the steady base flow can be computed in a two-dimensional domain in $x \cdot y$ plane including the bow shock ahead of the body. Subsequently, we extend the domain to span one wavelength of the target traveling mode, and disturb the flow to excite the traveling mode.

In this study, we consider planar freestream slow acoustics as they were found to be dominant in the wind tunnel environment. As preliminary, we assume that the wave vector has no component in the ydirection, and the perturbations are of the following form:

$$\begin{pmatrix} \rho' \\ u' \\ v' \\ r' \\ p' \end{pmatrix} = A_{\infty} M a_{\infty} \begin{pmatrix} M a_{\infty} \\ -\frac{k_{x}}{\sqrt{k_{x}^{2} + k_{z}^{2}}} \\ 0 \\ -\frac{k_{z}}{\sqrt{k_{x}^{2} + k_{z}^{2}}} \\ (\gamma - 1) M a_{\infty} \\ 1/M a_{\infty} \end{pmatrix} e^{i(k_{x}x + k_{z}z - \omega t)} + \text{c.c.}$$
(2)

where p', u', v', w', T', p' represent a small perturbation of density, velocity components in x, y, zdirections, temperature, and pressure, respectively. A_{∞} is the perturbation amplitude, ω is the angular frequency, k_x and k_z denote the wavenumbers in the x and z directions, respectively, and c.c. is the complex conjugate.

The dispersion relation for a slow acoustic wave is written as the following form:

$$\omega = k_x U_{\infty} + k_z W_{\infty} - M a_{\infty}^{-1} \sqrt{k_x^2 + k_z^2}$$
 (3)

where $U_{\infty} = Q_{\infty} \cos \Lambda$, $W_{\infty} = Q_{\infty} \sin \Lambda$. To excite a targeted traveling mode (ω_0, β_0), we need to specify $\omega = \omega_0$, $k_z = \beta_0$, and k_x can be calculated from the above equation.

The flow field is symmetrical about the x-z plane, allowing the computation to be confined to the upper half of the domain with symmetric boundary conditions applied on the symmetry plane. For the steady base flow, a third-order extrapolation boundary condition is used at the outlet. The wall is considered to be non-slip, isothermal wall. For the disturbed flow, a planar slow acoustic wave is superimposed on the steady base flow at the upper boundary. A buffer zone is set at the outlet to attenuate the upphysical reflections from the boundary. A periodic boundary condition is employed in the spanwise direction.

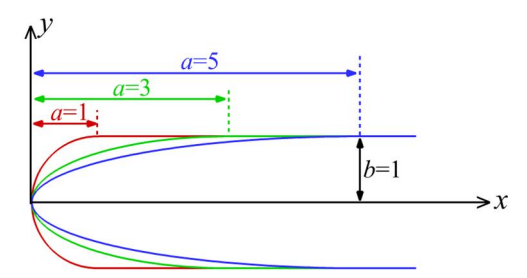


Fig 1. Sketch of the models investigated.

To accurately capture the interaction of the freestream disturbances with the shock, we carefully design the grid align one gridline with the bow shock. To achieve this goal, we first precompute the base flow using a coarse grid, then extract the bow shock and establish the fine grid. Subsequently, we compute both the steady base flow and disturbed flow using the fine grid. The meshes are very fine near the nose and gradually become coarser downstream. In the wall-normal direction, 302 points are deployed with the grids clustered in the shock region and near the wall, and at least 120 points are used within the boundary layer. The computational domain in the x-direction is taken as 10, with 398 and 610 points deployed for the cylindrical case (a=1) and ellipsoidal cases (a=3, 5), respectively. In the nose region where $x \le 1$, approximately 80 and 200 grid points are used for the respective configurations. In the spanwise direction, 31 points are used for all three cases.

HiSST-2025-XXXX Page | 3 Leading-Edge Shape Effects on Hypersonic Crossflow Receptivity to Slow Acoustic Waves in Swept Flat Plates Copyright ©

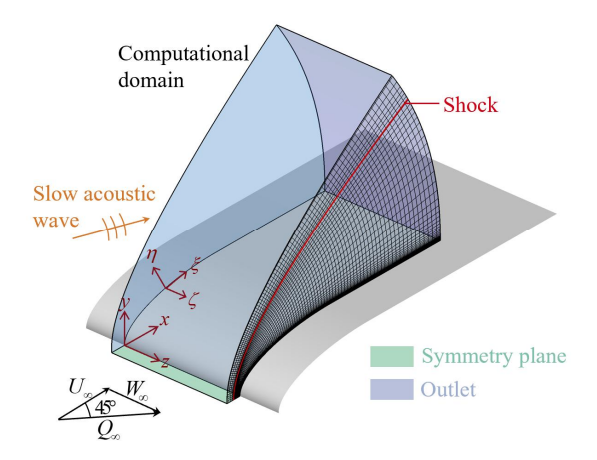


Fig 2. Schematic diagram of the computational setup with the computational domain and the coordinate systems.

3. Base flow and linear stability analysis

3.1. Base flow

Fig. 3 illustrates the pressure contours of the steady base flow for the three cases, clearly showing the detached shock. As a increases from 1 to 5, the detached shock wave moves closer to the nose. Fig. 4 depicts the wall pressure variations along the x-axis for the three cases, revealing a region of favorable pressure gradient near the nose, which can result in significant crossflow. The favorable pressure gradient region becomes larger as a increases from 1 to 5.

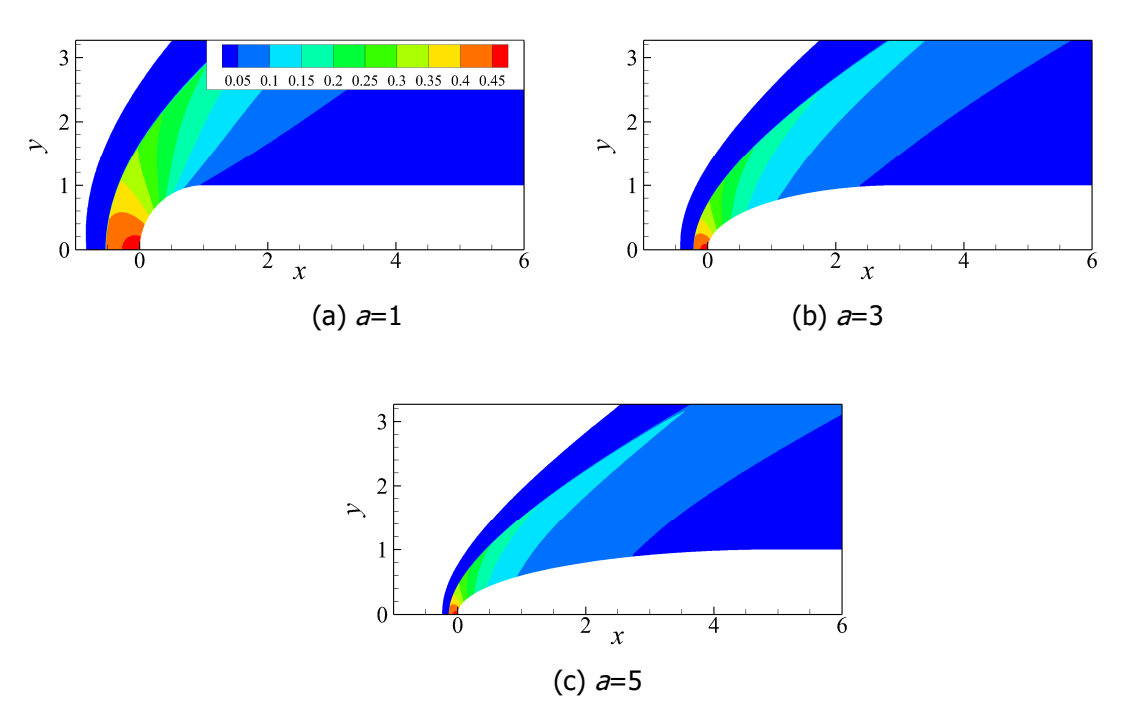


Fig 1. Pressure contours of the base flow.

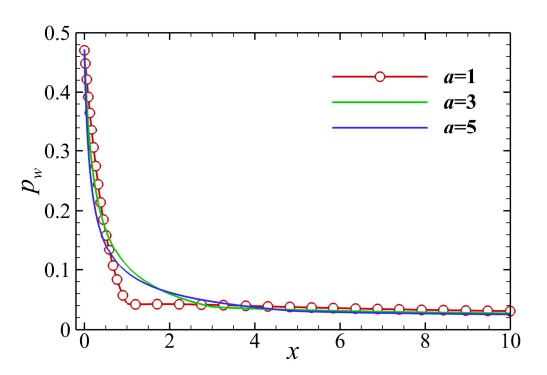


Fig 2. Variation of wall pressure along x.

3.2. Linear stability analysis

Linear stability analysis was conducted to examine the stability properties of the boundary layers for the three cases. Fig. 5 depicts the neutral stability curves for the crossflow instability mode with different spanwise wavenumbers, namely, β =5, 7, 9. This analysis begins at x=1, where the chordwise surface curvature is not included for the case with a=1. In contrast, for the cases with a=3 and 5, the chordwise curvature of the ellipsoidal nose is present, affecting the stability characteristics. As shown in Fig. 8, for instability modes with positive frequencies, the existence of chordwise curvature has a minimal effect on the neutral stability curves. Conversely, for modes with negative frequencies, the neutral curves considering surface curvature exhibit a contraction in the nose region for both the cases with a=3 and 5, suggesting a stabilizing influence on the crossflow instability.

We choose the mode with (ω,β) =(1,7) as the target traveling wave in the subsequent receptivity investigations. Small variations in the frequency and spanwise wavenumber should not affect the receptivity mechanisms. Fig. 6 presents growth rate and N-factor curve of the mode with (ω,β) =(1,7) for the three cases. As can be seen, the maximum growth rate and N-factor decrease for the cases with a increasing from 1 to 5. Moreover, the surface curvature of the nose exhibits a more stabilizing influence on the traveling mode for the case with a=5 compared to that with a=3. Overall, at the downstream location of x=7, corresponding to a dimensional value of 70 mm, the N-factors reach values ranging from 4 to 5.4, with the higher value occurring for cases with a smaller a. This is consistent to previous experimental observations on hypersonic swept wings.

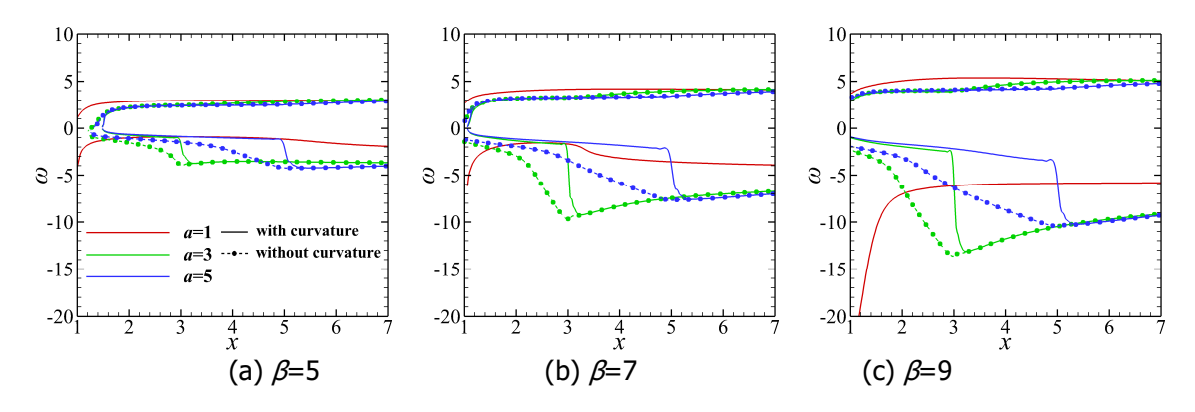


Fig 3. Neutral curves of crossflow instability with different spanwise wavenumbers.

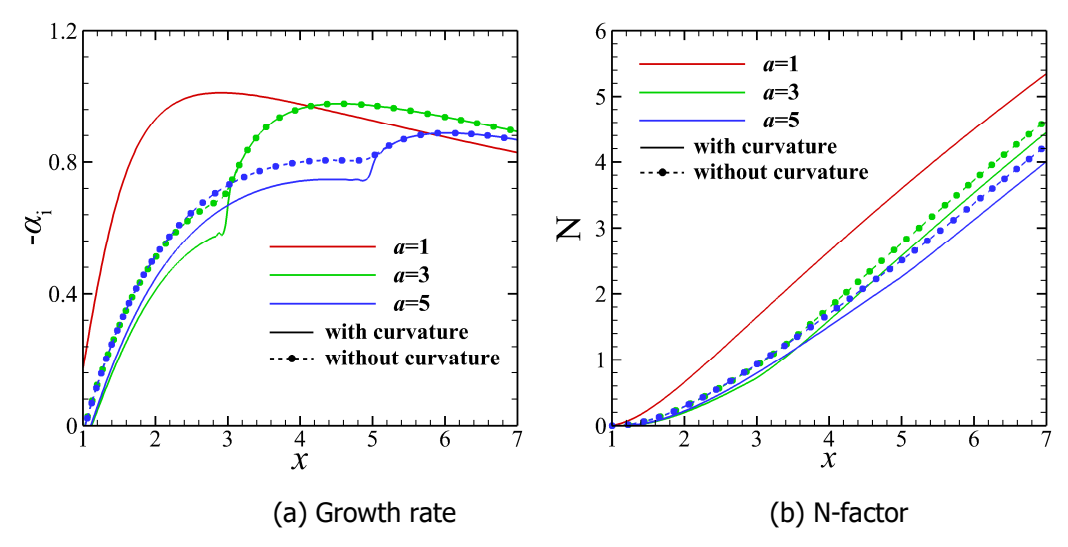


Fig 4. Growth rate and N-factor curves of the crossflow traveling mode with $(\omega,\beta)=(1,7)$.

4. Receptivity investigations

We investigate the excitation of the target traveling mode, (ω,β) =(1,7), by superimposing planar freestream slow acoustic waves at the upper boundary of the domain. The forcing frequency corresponds to a dimensional frequency of 14.8 kHz. The acoustic pressure amplitude A_{∞} taken to be 10^{-6} . The disturbed computation ends until all flow quantities at each grid point reach a completely periodic state.

Fig. 7 illustrates instantaneous pressure fluctuation contours for the three cases within the z=0 plane. As can be seen, the interaction between the freestream slow acoustic disturbances and the shock gives rise to stronger pressure fluctuations behind the shock. Near the wall, a wave-like pattern emerges originating from close to the leading edge. As will be discussed subsequently, these wave patterns correspond to the excited traveling mode. Furthermore, a localized scattering effect can be observed due to the surface curvature discontinuity, which slightly distorts the wave front; this phenomenon is more pronounced for the case with a=1 compared to the other two cases.

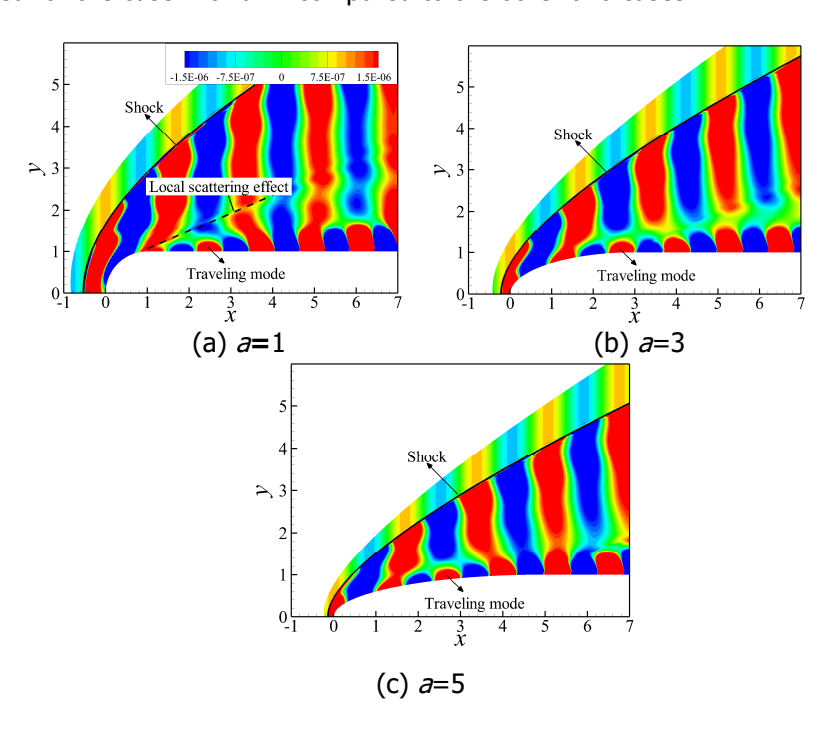


Fig 5. Instantaneous pressure fluctuation contours.

To validate the excitation of the target traveling mode, we extract the disturbance shape functions from DNS and compare them with those predicted by LST and PSE. To initialize the PSE computation, a traveling mode predicted by LST was used as the inlet condition. To facilitate the comparison, the disturbance shape functions obtained through the different approaches were normalized by the maximum modulus of chordwise velocity perturbation ($|\hat{u}|$) within the boundary layer. As shown in Fig.8, the DNS results demonstrate excellent agreement with the LST and PSE predictions starting from x=1.5, indicating that the traveling mode is excited, and the excitation occurs very close to the leading edge. Particularly, the PSE approach provides a closer match in the nose region compared to LST due to its ability to account for the non-parallelism of the mean flow.

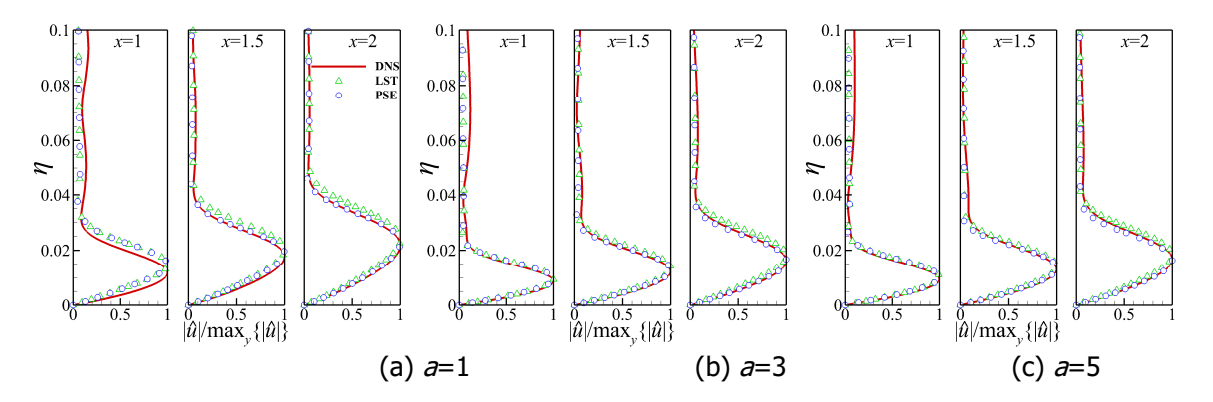


Fig 6. Chordwise velocity perturbation shape functions of the disturbances from DNS in comparison of those of the traveling mode given by LST and PSE at different x-locations.

Fig. 9 compares the instantaneous wall pressure fluctuations with the disturbance amplitude evolution obtained using LST and PSE. The LST and PSE computations start with the traveling mode at x=1, and the initial amplitude is adjusted to match the downstream disturbance amplification obtained in DNS as much as possible. As is shown, the LST and PSE results are nearly identical, both demonstrating excellent agreement with the DNS result. This agreement further confirms that the traveling mode is excited, and the entire evolution remains within the linear regime. Among the three cases, the boundary layer exhibits a weaker response for the cases with increasing a from 1 to 5, consistent with the amplification trends indicated by the LST N-factor curves. To gain an insight into the receptivity mechanism, the growth rate and wavenumber can be obtained by analyzing the wall pressure fluctuations via Fourier analysis:

$$p'_{w}(x,z,t) = \hat{p}(x)e^{i(\beta z - \omega t)} + \text{c.c.}$$
(4)

$$\alpha(x) = \alpha_{r} + i\alpha_{i} = \frac{1}{i\hat{p}(x)} \frac{\partial \hat{p}(x)}{\partial x}$$
 (5)

The phase speed can be computed by

$$c = \frac{\omega}{\sqrt{\alpha_{\rm r}^2 + \beta^2}} \tag{6}$$

Fig. 10 illustrates the variations of the phase speed and growth rate in comparison of the results given by LST and PSE. To indicate the influence of the wall curvature discontinuity, the geometry is depicted at the bottom of the figures. It can be observed that for the case with a=1, the phase speed and growth rate variation curves exhibit large fluctuations near the surface curvature discontinuity, and align with those predicted by LST and PSE downstream. The rapid variation indicates a localized scattering effect on the excited traveling mode due to the surface curvature discontinuity. For the cases with a=3 and 5, the phase speed and growth rate given by LST and PSE show good agreement with the DNS results starting from x=1-2, with a small local fluctuation occurring near the position of the surface curvature discontinuity. This fluctuation is less pronounced with the increasing a of the nose configurations, suggesting a weaker local scattering effect. Overall, the excitation of the traveling mode is very close to the leading edge, which is more likely attributable to the rapidly varying mean flow, rather than the presence of surface curvature discontinuity.

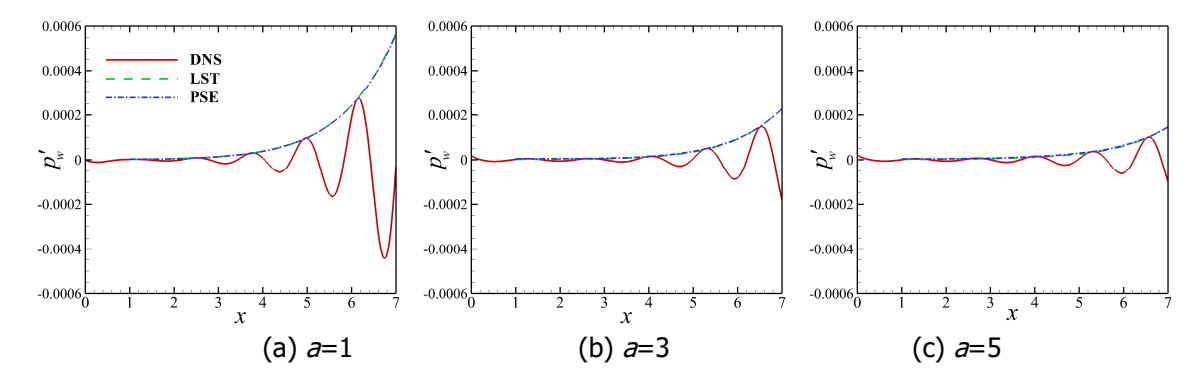


Fig 7. Comparisons of the wall pressure fluctuation amplitudes between DNS, LST and PSE.

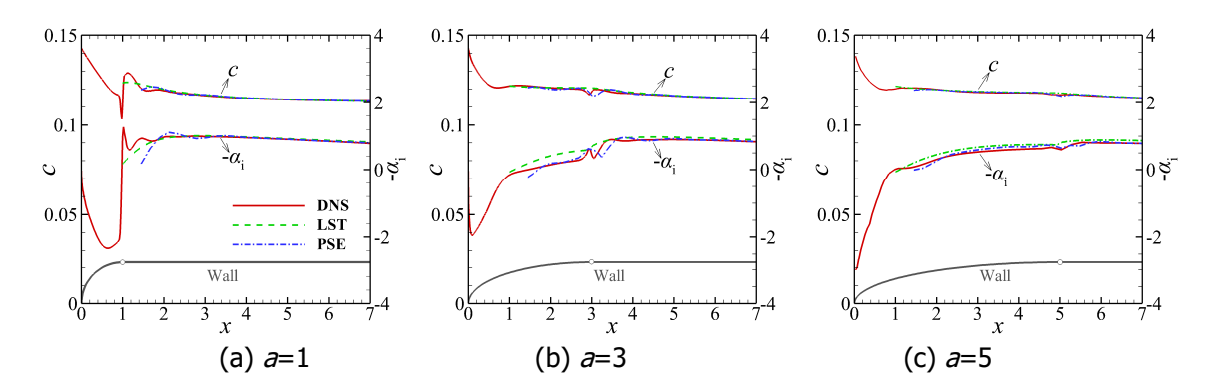


Fig 8. Phase speed and growth rate of the wall pressure fluctuation and those of the crossflow traveling mode.

To directly compare the receptivity efficiency for the three cases, we plotted the wall pressure fluctuation amplitudes in a logarithmic scale, as illustrated in Fig.11. PSE results are also included for comparison. If we follow the PSE curves upstream, the minimum value of the amplitude curve corresponds to the initial amplitude of the excited traveling mode. As is evident, the initial amplitudes for the cases with a=3 and a=5 are very close, noticeably larger than that with a=1. This indicates that the less blunt ellipsoidal cases have a stronger receptivity efficiency. However, at downstream location beyond x=2, the case with a=1 achieves the largest amplitude among the three cases. Further downstream beyond x=4, it is clear that as the nose bluntness increases, the traveling mode attains a larger amplitude due to a larger amplification rate.

To quantify the receptivity efficiency, the receptivity coefficient based on wall pressure perturbations is defined as the ratio of the initial amplitude of the excited traveling mode to the freestream acoustic pressure:

$$C = \frac{A_0}{A_{ro}} \tag{7}$$

We find that the receptivity coefficient C is 3.26, 4.89, and 4.43 for the cases with a=1, 3, and 5, respectively. The differences in receptivity among these cases can be reflected by ΔN , which is defined as follows:

$$\Delta N = \ln \frac{C_i}{C_0} \tag{8}$$

where the subscript 'i' denotes the target case and subscript '0' denotes the baseline, which was chosen to be the case with a=1. To assess the extent to which receptivity affects the overall disturbance amplification, we define

$$\lambda = \frac{\Delta N}{N_{\text{max}}} \tag{9}$$

where N_{max} is the maximum N-factor obtained by LST. Clearly, a larger λ indicates a larger influence of receptivity on the overall disturbance evolution. We find that λ =9.1% and 7.7% for the cases with a=3 and 5, respectively. In general, these values are small, suggesting that the disturbance evolution is

largely determined by the boundary-layer instability, and the differences in receptivity for varying nose bluntness have a less significant effect on the disturbance evolution for the cases investigated.

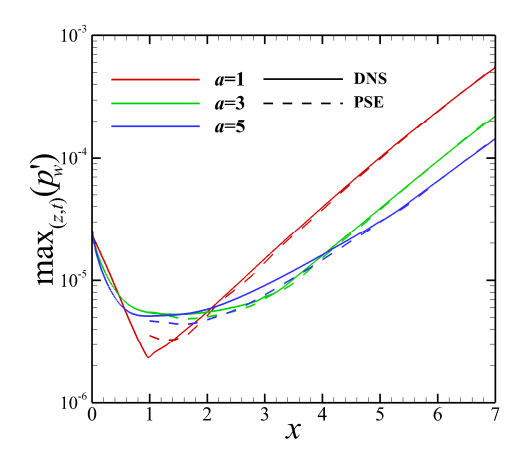


Fig 9. Comparisons of the wall pressure perturbation amplitudes of the three cases.

5. Conclusions

Three distinct leading-edge geometries were investigated: a cylindrical nose with sharp curvature discontinuity, and two ellipsoidal noses featuring smoother curvature transitions. Direct numerical simulations (DNS), combined with linear stability theory (LST) and parabolized stability equations (PSE), are used to resolve the receptivity process and downstream disturbance development for a target traveling mode. The main conclusions are as follows:

- (1) The steady base flow shows that increased nose bluntness leads to a larger favorable pressure gradient in the nose region, which significantly impacts boundary layer instability. Linear stability analysis reveals that nose bluntness promotes amplification of the traveling mode, consistent with previous studies on swept wing boundary layers.
- (2) The receptivity investigations reveal that the traveling mode is excited primarily within the rapidly varying mean flow region near the leading edge. Importantly, the abrupt curvature discontinuity of the cylindrical nose induces localized scattering effects on disturbances, while smoother ellipsoidal noses mitigate this scattering due to their gradual curvature transitions.
- (3) Receptivity coefficients indicate that the cylindrical nose exhibits smaller values compared to the ellipsoidal cases. However, this reduced initial amplitude of the traveling mode through receptivity is offset by enhanced downstream instability amplification. Specifically, the stronger pressure gradient associated with the cylindrical nose promotes faster disturbance growth, ultimately leading to larger disturbance amplitudes downstream.

References

- 1. Bertin, J.J., Cummings, R.M.: Fifty years of hypersonics: where we've been, where we're going. Prog. Aerosp. Sci. 39(6–7), 511–536 (2003)
- 2. Saric, W.S., Reed, H.L., Kerschen, E.J.: Boundary-layer receptivity to freestream disturbances. Annu. Rev. Fluid Mech. 34(1), 291–319 (2002)
- 3. Corke, T., Arndt, A., Matlis, E., et al.: Control of stationary cross-flow modes in a Mach 6 boundary layer using patterned roughness. J. Fluid Mech. 856, 822–849 (2018)
- 4. Juliano, T.J., Borg, M.P., Schneider, S.P.: Quiet tunnel measurements of HIFiRE-5 boundary-layer transition. AIAA J. 53(4), 832–846 (2015)
- Kosinov, A.D., Kolosov, G.L., Semionov, N.V., et al.: Linear development of controlled disturbances in the supersonic boundary layer on a swept wing at Mach 2. Phys. Fluids 28(6), 064101 (2016)

HiSST-2025-XXXX Page | 9
Leading-Edge Shape Effects on Hypersonic Crossflow Receptivity to Slow Acoustic Waves in Swept Flat Plates Copyright ©
2025 by author(s)

- 6. Placidi, M., Ashworth, R., Atkin, C.J., et al.: Effect of environmental disturbances on crossflow instability. Exp. Fluids 64(2), 37 (2023)
- 7. Craig, S.A., Saric, W.S.: Crossflow Instability in a Hypersonic Boundary Layer. J. Fluid Mech. 808, 224–244 (2016)
- 8. Wan, B.B., Tu, G.H., Yuan, X.X., et al.: Identification of Traveling Crossflow Waves under Real Hypersonic Flight Conditions. Phys. Fluids 33(4), 044110 (2021)
- 9. Paredes, P., Choudhari, M.M., Li, F., et al.: Nose-tip bluntness effects on transition at hypersonic speeds. J. Spacecr. Rockets 56(2), 369–387 (2019)
- 10. Archambaud, J.P., Louis, F., Séraudie, A., et al.: Natural transition in supersonic flows: flat plate, swept cylinder, swept wing. In: 34th AIAA Fluid Dynamics Conference and Exhibit, Portland, Oregon. AIAA (2004)
- 11. Niu, H.B., Yi, S.H., Liu, X.L., et al.: Experimental investigation of nose-tip bluntness effects on the hypersonic crossflow instability over a cone. Int. J. Heat Fluid Flow 86, 108746 (2020)
- 12. Paredes, P., Scholten, A., Choudhari, M.M., et al.: Modal Instabilities over Blunted Cones at Angle of Attack in Hypersonic Flow. J. Spacecr. Rockets 60(4), 1188–1200 (2023)